In Situ Initiation of East Pacific Easterly Waves in a Regional Model

ADAM V. RYDBECK[a] AND ERIC D. MALONEY

Department of Atmospheric Science, Colorado State University, Fort Collins, Colorado

GHASSAN J. ALAKA JR.

Cooperative Institute for Marine and Atmospheric Studies, University of Miami, and NOAA/Atlantic Oceanographic and Meteorological Laboratory/Hurricane Research Division, Miami, Florida

(Manuscript received 20 April 2016, in final form 20 October 2016)

ABSTRACT

The in situ generation of easterly waves (EWs) in the east Pacific (EPAC) is investigated using the Weather Research and Forecasting (WRF) Model. The sensitivity of the model to the suppression of EW forcing by locally generated convective disturbances is examined. Specifically, local forcing of EWs is removed by reducing the terrain height in portions of Central and South America to suppress robust sources of diurnal convective variability, most notably in the Panama Bight. High terrain contributes to the initiation of mesoscale convective systems in the early morning that propagate westward into the EPAC warm pool. When such mesoscale convective systems are suppressed in the model, EW variance is significantly reduced. This result suggests that EPAC EWs can be generated locally in association with higher-frequency convective disturbances, and these disturbances are determined to be an important source of EPAC EW variability. However, EPAC EW variability is not completely eliminated in such sensitivity experiments, indicating the importance for other sources of EW forcing, namely, EWs propagating into the EPAC from West Africa. Examination of the EW vorticity budget in the model suggests that nascent waves are zonally elongated and amplified by horizontal advection and vertical stretching of vorticity. Changes in the mean state between the control run and simulation with reduced terrain height also complicate interpretation of the results.

1. Introduction

Tropical cyclones observed in nature always originate from preexisting atmospheric disturbances. In the east Pacific (EPAC), many studies have hypothesized that the most prevalent precursor disturbances are easterly waves (EWs) originating over Africa (Simpson et al. 1969; Frank 1970; Shapiro 1986; Avila and Pasch 1992, 1995; Blake and Pasch 2010; Blake and Kimberlain 2013). This study supports the alternate view that EWs can be initiated locally in the EPAC. Mechanisms of in situ EW and tropical cyclone (TC) initiation in the EPAC have previously been suggested, such as intertropical convergence zone (ITCZ) breakdown (Ferreira and Schubert 1997), barotropically unstable gap wind jets (Mozer and Zehnder 1996), inertial instabilities arising from cross-equatorial pressure gradients (Toma and Webster 2010a,b), and growth of vorticity noise by barotropic conversion in the presence of a suitable EPAC basic state (Maloney and Hartmann 2001; Hartmann and Maloney 2001). We hypothesize that intense convective forcing originating around the Panama Bight is able to seed EWs in the EPAC. The mechanism proposed herein is distinct from previous ideas of remote and in situ forcing, while not excluding them.

Tropical EWs are off-equatorial low pressure convective systems that migrate westward at 5–11 m s^{-1} in tropical easterlies. EWs are characterized by zonal wavelengths of 2000–4400 km and periods of 3–5 days (Tai and Ogura 1987; Serra et al. 2008) and have maximum meridional wind anomalies near 850–600 hPa. Rydbeck and Maloney (2014) showed that EWs in the EPAC are strongly energized by 1) conversions of perturbation available potential energy to perturbation kinetic energy and 2) barotropic conversions. Rydbeck and Maloney (2015) showed that the distribution of

[a] Current affiliation: Ocean Sciences Division, U.S. Naval Research Laboratory, Stennis Space Center, Mississippi.

Corresponding author e-mail: Adam V. Rydbeck, adam.rydbeck@gmail.com

DOI: 10.1175/JAS-D-16-0124.1

convection in growing EWs supports a southwest-to-northeast horizontal tilt of the wave. Easterly waves with such tilts intensify in the presence of cyclonic shear of the mean zonal winds. This process is the leading component of the barotropic energy conversion term in the perturbation kinetic energy budget. The present study investigates the origins of EW vorticity anomalies in the EPAC, building on the previous work of Rydbeck and Maloney (2014, 2015).

EWs have been actively identified and recorded near and within the intra-Americas seas since at least 1887 (Dunn 1933). However, the salient dynamical and convective features of EWs are often difficult to track across the tropics. When the convective signals and wind circulations of EWs are undetectable, as often occurs over the dry and hostile Caribbean, many observational studies have used subjective measures to track EWs. For example, some studies have assumed a continuous EW trajectory across the Atlantic and Caribbean, even when the wave is not observable (e.g., Avila and Pasch 1995; Beven et al. 2005).

However, Molinari et al. (1997) questioned the existing paradigm of continuous EW propagation across the tropical Atlantic into the EPAC, suggesting that EWs can be characterized as dispersive Rossby wave packets. Under this consideration, EWs would dissipate in the absence of deep convection before reaching the Caribbean, Gulf of Mexico, or EPAC. Supporting this hypothesis, previous work has shown that the western tropical Atlantic and the western Caribbean are indeed regions of significant EW lysis (Thorncroft and Hodges 2001; Serra et al. 2010). Although some EWs do clearly traverse the Atlantic into the EPAC (i.e., Shapiro 1986), many studies have suggested that the primary energy sources for EWs in the EPAC are local to the EPAC (Maloney and Hartmann 2001; Aiyyer and Molinari 2008; Serra et al. 2010; Rydbeck and Maloney 2014). If a large number of EWs do fully decay in the Atlantic and Caribbean in the absence of deep convection, the initiation of in situ EWs would be necessary to support the observed number of EPAC TCs.

Hartmann and Maloney (2001) used a simple barotropic model forced with vorticity noise to suggest that EPAC EWs could be generated in situ. In the model, the EWs generated are similar in horizontal structure, amplitude, and perturbation kinetic energy distributions to those from reanalysis. Their results suggest that in situ EW initiation and growth in the EPAC is possible given sufficient forcing and a favorable EPAC background state. Supporting the contention of Hartmann and Maloney (2001), the EW energy budget analysis of Rydbeck and Maloney (2014) suggested that a finite-amplitude disturbance could develop into a robust EPAC EW in approximately 1.5–2.5 days from barotropic and perturbation available potential energy to perturbation kinetic energy conversions.

Velasco and Fritsch (1987) noted a direct relationship between several EPAC tropical cyclogenesis occurrences and mesoscale convective vortices associated with mesoscale convective complexes originating over South America. To provide another example, TC Elida formed in the EPAC on 11 July 2008 approximately 315 nautical miles south-southeast of Puerto Angel, Mexico, and eventually reached hurricane strength on 14 July. TC Elida reached a peak intensity of 90 knots (kt; 1 kt = 0.51 m s^{-1}) on 16 July and gradually weakened to below hurricane strength on 18 July. As previously mentioned, most TCs in the EPAC are said to form in association with waves propagating from Africa. TC Elida did not support this paradigm in that the cyclone formed in association with a tropical wave that first appeared near Central America (Blake and Pasch 2010).

As can be seen in a time–longitude diagram of EPAC 700-hPa vorticity and precipitation in Fig. 1 (see section 2 for description of data), no strong predecessor signals in the total precipitation and vorticity fields are present outside the EPAC prior to the formation of TC Elida. The tropical wave that led to the formation of TC Elida is only traceable back to the coast of Central and South America, in the region known as the Panama Bight. Westward-propagating mesoscale convective systems with diurnal periods are well known to routinely occur in the Panama Bight (Mapes et al. 2003a) and are evident in the total precipitation field shown in Fig. 1. Some of these diurnal pulses are stronger than others. These diurnal mesoscale convective systems typically propagate to the west at 15–20 m s^{-1}. The precise origin of the EW responsible for seeding TC Elida is unknown, but a hypothesis on the formation of EWs near the Panama Bight is presented in this paper.

A goal of the current study is to investigate the robust forcing associated with the convective forcing near the Panama Bight and its role in EW formation. We hypothesize that westward-propagating convective disturbances originating near the Panama Bight help to initiate and grow EPAC EWs. Many previous studies have noted that EPAC EWs appear to originate near the coasts of Panama and Colombia, with little to no preceding signals located in the Atlantic Ocean (Nitta and Takayabu 1985; Tai and Ogura 1987; Serra et al. 2008; Toma and Webster 2010b; Serra et al. 2010; Rydbeck and Maloney 2014). In that same region (i.e., the coastal region just west of the Colombian Andes), a large number of mesoscale convective complexes are known to occur during boreal summer (Velasco and Fritsch 1987). In fact, that same region has been shown to have

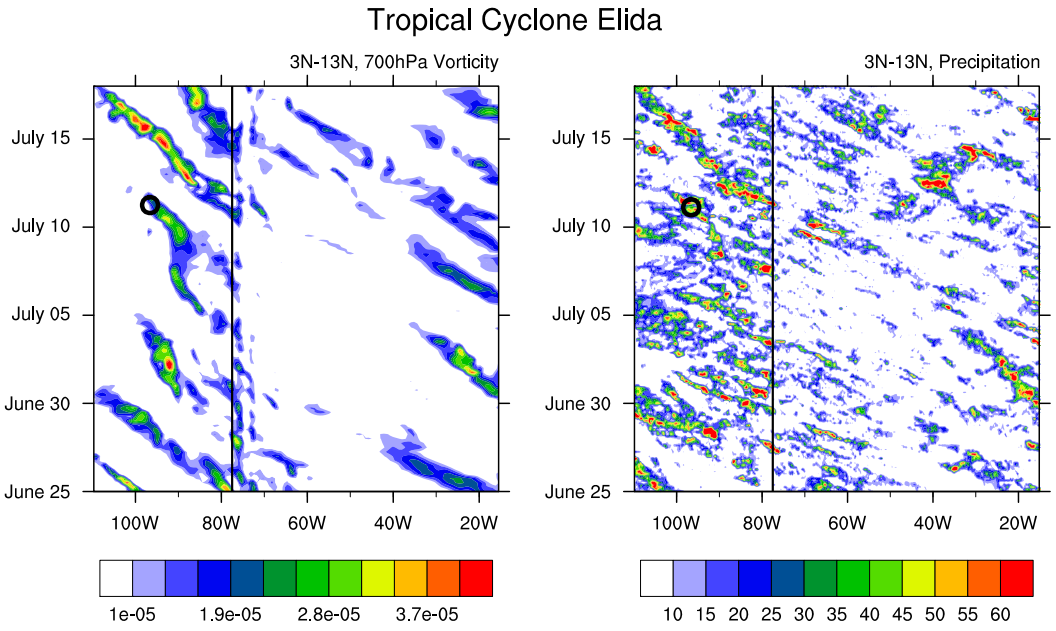

FIG. 1. Time–longitude sections of (left) 700-hPa relative vorticity (s^{-1}) and (right) precipitation (mm day^{-1}) averaged from 3° to 13°N are shown. The vertical black line indicates the longitude of the Pacific coast of South America. The black circle shows the longitude and time of genesis for Tropical Cyclone Elida.

the highest occurrence of organized deep convection on the planet based on the highly reflective cloud dataset, where convective clusters in the Panama Bight propagate westward diurnally (Mapes et al. 2003a). Mapes et al. (2003b) and Warner et al. (2003) used a regional model to show that convection is initiated in this region when temperature anomalies associated with westward-propagating gravity waves cool a warm capping layer near 850 hPa, allowing the convective available potential energy of the column to be realized. The gravity waves and attendant convection were found to be strongly dependent on the presence of the Andes Mountains in Colombia. The westward-propagating mesoscale convective systems in the Panama Bight ceased when the mountains were removed in the model, a fact that is utilized in sensitivity tests in the current study.

In this study, a regional model is utilized to better understand the underlying mechanisms of EW formation in the EPAC. In particular, the local forcing of EPAC EWs by the strong and westward-propagating mesoscale convective systems in the Panama Bight is investigated. The degree to which these mesoscale convective systems seed EWs is investigated by suppressing the terrain-induced precipitation variability in the model. Section 2 describes the regional model used for this study, the methods for suppressing mesoscale convective systems near the Panama Bight, and the reanalysis and observational data used for model comparison. Section 3 examines the model simulations to better understand the sensitivity of EPAC EWs to local convective forcing. Section 4 expands on this process-level investigation of in situ EW generation by analyzing the EW vorticity budget. Section 5 presents some discussion and conclusions.

2. Model setup and simulations

The Advanced Research Weather Research and Forecasting (WRF) Model, version 3.4.1, (Skamarock and Klemp 2008) is used to investigate EWs in this study. Previous studies have successfully employed WRF to study tropical phenomena in regional climate simulations (e.g., Tulich et al. 2011; Mallard et al. 2013; Jin et al. 2013; Alaka 2014; Kim et al. 2015). Multiple model parameterization configurations/combinations were tested in WRF using month-long sensitivity tests to find the most suitable set to simulate tropical synoptic variability and the mean atmosphere in the EPAC. The settings that best represented the variability and mean state of the EPAC include the Kain–Fritsch cumulus parameterization (Kain 2004), the WRF single-moment 6-class microphysics scheme (Hong and Lim 2006), the Community Atmosphere Model (CAM; Collins et al. 2004) shortwave and longwave radiation, the Noah land surface model, and the Yonsei University (YSU; Hong et al. 2006) planetary boundary layer parameterization. These parameterization settings are utilized in all

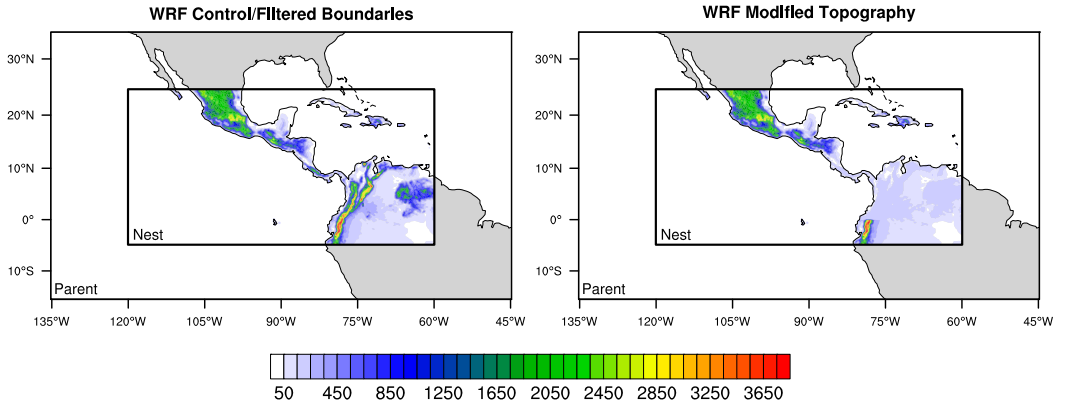

FIG. 2. Parent and nested domains of (left) the WRF control/filtered boundaries and (right) the WRF modified topography simulations are shown. Terrain height (m; color contours) of the nested domain is shown for the respective simulations.

simulations. Other parameterizations tested include the Grell 3 cumulus parameterization, the WRF double-moment 6-class microphysics scheme (Lim and Hong 2010), the Thompson microphysics scheme (Thompson et al. 2008), and the Rapid Update Cycle (RUC) land surface model. Many of the combinations of parameters generated excessive amounts of mean precipitation or underrepresented EPAC EW activity.

Simulations are conducted for the summer seasons (May–November) of 2000–09 using lateral and boundary forcings from the European Centre for Medium-Range Weather Forecasts interim reanalysis (ERA-Interim) (0.75°; Dee et al. 2011). SSTs and lateral boundary conditions are updated every 6 h. The outer- and inner-nest grid spacings are 54 and 18 km, respectively, and encompass much of the Caribbean, Gulf of Mexico, and EPAC warm pool, as shown in Fig. 2. The model has 31 vertical levels with the top at 50 hPa. The inner domain is one-way nested within the parent domain.

Using the WRF, two simulations are performed: a control simulation and modified topography simulation. The control simulation is run as previously described, with no modifications. In the modified topography simulation, topography associated with the local forcing of westward-propagating mesoscale convective systems in the Panama Bight is modified such that elevations do not exceed 400 m over particular areas in the nested domain. The terrain height for the control and modified topography simulations are shown in Fig. 2. Modifying the topography is similar to the approach used in Mapes et al. (2003b) to decrease the rainfall variability in the Panama Bight. The success of this approach at minimizing rainfall variability in the region is examined later. The modified topography simulation is not sensitive to reasonable changes in the terrain-height threshold. However, it is sensitive to the areal extent of the flattened terrain. Orographically generated convective systems are present in both northern South America and portions of Central America in the model and require the flattening of terrain in both regions to sufficiently suppress diurnal convective activity to the east of the EPAC warm pool.

The model simulations are compared with 6-hourly, 0.75° ERA-Interim fields as well as 6-hourly, 0.25° Tropical Rainfall Measuring Mission (TRMM; Kummerow et al. 2000) 3B42 precipitation data from the same summer seasons as the model integrations. The National Climatic Data Center (NCDC) outgoing longwave radiation (OLR) daily climate data record is also used (Lee 2014; NOAA 2014). The 1° × 1° grid spaced data are linearly interpolated to 6-hourly time steps and are largely consistent with 6-hourly OLR data from ERA-Interim when composited for EW periods. When comparing vorticity between the model simulations and observations, model winds have been linearly interpolated to the reanalysis grid before relative vorticity is computed such that the vorticity magnitudes may be uniformly compared.

3. Modeling results on local forcing and EWs

EPAC EWs are known to be sensitive to changes in the background state of the atmosphere (e.g., Molinari and Vollaro 2000; Maloney and Hartmann 2001; Aiyyer and Molinari 2008; Crosbie and Serra 2014; Rydbeck and Maloney 2014, 2015). Therefore, in order to properly simulate EPAC EWs, the background state must be reasonably represented in the model. Examples of important background features include the Caribbean low-level jet and its extensions into the northern EPAC through the mountain gaps of Central America, the location and intensity of the ITCZ, low-level westerly winds in the EPAC warm pool, and meridional shear of the mean zonal winds. These features of the mean state

have been suggested to be dynamically and thermodynamically important to the initiation and maintenance of EWs as well as TCs in the EPAC, and some aspects are discussed to confirm the model's suitability for simulating EWs.

The mean precipitation and 10-m surface winds for both model simulations and observations are shown in Fig. 3. In observations (top panel), a precipitation maximum of 16 mm day^{-1} is located near the Panama Bight, just off the Pacific coasts of Colombia and Panama. The maximum extends to the west-northwest and defines the boreal summer ITCZ in the EPAC. Much of the ITCZ is embedded within a westerly component of the surface flow. The westerly component is generally stronger near the Central and South American coasts. A weakening of the ITCZ on its northern flank is apparent near the Costa Rica dome (11°N, 88°W), a region of strong ocean upwelling due to Ekman divergence forcing on the cyclonic shear side of the Papagayo jet that results in anomalously cooler SSTs (Chelton et al. 2000a,b). The Papagayo jet is often considered to be an extension of the easterly Caribbean low-level jet across Lake Nicaragua that is still well defined in the surface winds.

The surface winds and precipitation for the WRF control (Fig. 3, middle panel) and modified topography simulations (Fig. 3, bottom panel) are also shown. The control simulation realistically represents some basic features of the large-scale precipitation and circulation pattern such as the westerly component of the low-level winds, Caribbean low-level jet, west-northwest orientation of the ITCZ, and a local maximum of precipitation near and to the west of the Panama Bight. Mean precipitation rates in the ITCZ are greater than observed and shifted to the north by a few degrees. The contour interval is 2 mm day^{-1} for the WRF control simulation and 1 mm day^{-1} for observations. In other studies utilizing regional models, similar biases of the EPAC climatology have been noted (Small et al. 2011; Rydbeck et al. 2013). Near the Costa Rican coast, precipitation rates are much greater than observed and likely associated with increased southerlies as well as a local intensification of convective disturbances near the terminus of the Papagayo jet in the east Pacific.

In the WRF modified topography simulation, the Caribbean low-level jet is well represented, precipitation rates are comparable to those observed from TRMM, and the precipitation hole near the Costa Rica dome is well resolved. Westerly wind speeds within and just to the south of the ITCZ are reduced in the WRF modified topography simulation compared to observations. The reduction in westerly winds and cyclonic vorticity within the ITCZ (figure not shown) is partly considered to be a consequence of suppressing orographically generated

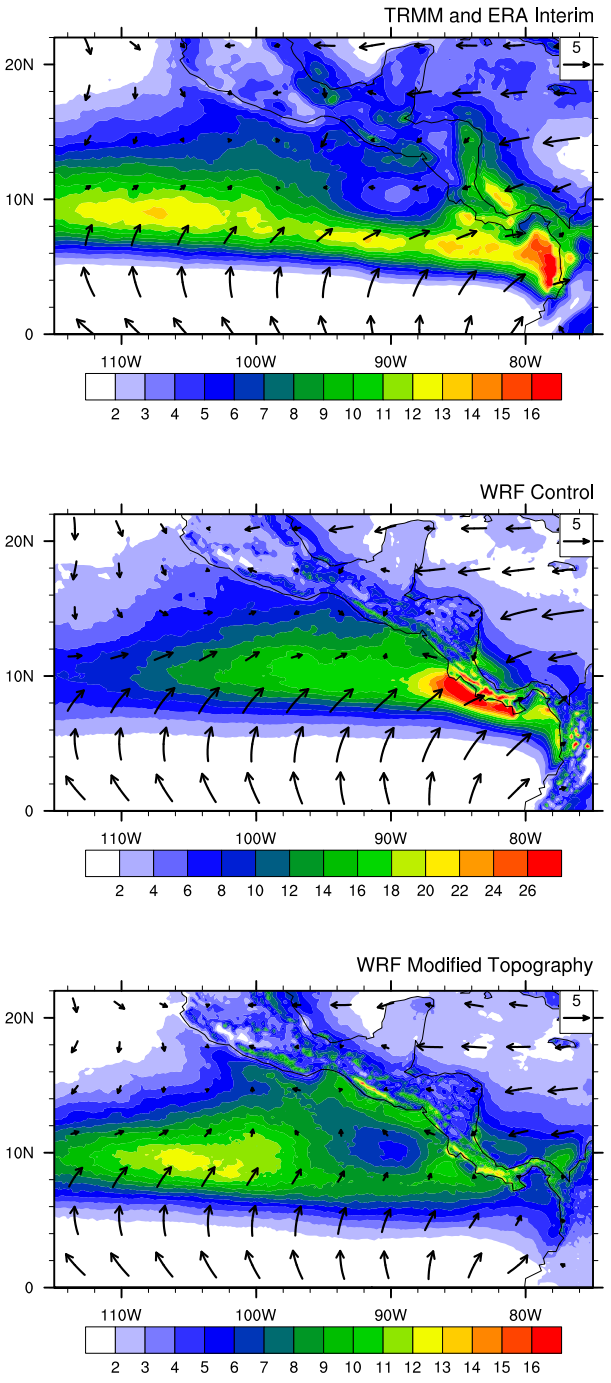

FIG. 3. Mean precipitation (mm day^{-1}; color contours) and 10-m surface winds (m s^{-1}; wind vectors) for the May–November 2000–09 period for (top) ERA-Interim and TRMM, (middle) WRF control, and (bottom) WRF modified topography are shown. Reference wind vector is located in the upper-right corner of each panel. The contour values for the WRF control simulations are larger than for observations.

mesoscale convective systems and, as will be discussed below, easterly waves in the region (see Fig. 7). Holton et al. (1971, 275–276) stated, ''The concentration of precipitation, vorticity, and divergence which we call the ITCZ is not simply a steady atmospheric state, but should be viewed as a consequence of the properties of large-scale equatorial wave disturbances.'' Under this consideration, suppressing easterly waves would also reduce the mean precipitation and cyclonic vorticity of the ITCZ, as shown in the WRF modified topography simulation. While the considerations of Holton et al. (1971) are valid, significant changes to the mean state independent of changes in easterly wave variability cannot be excluded in the WRF modified topography simulation and may complicate the interpretation of the sensitivity tests. A prominent and localized difference between TRMM and the WRF modified topography simulation is the absence of the local precipitation rate maximum along the coast of Central and South America. This is an expected result from modifying the topography and eliminating much of the high-frequency convective variability in the region. We will show below that this absence of strong mesoscale convective forcing along the coast has important consequences for the magnitude of easterly wave variability simulated in the model.

The suppression of diurnal convective activity near the coasts of Central and South America is further confirmed by analyzing composite time–longitude plots of the diurnal cycle of precipitation averaged from 3° to 11°N shown in Fig. 4. The dashed line in each panel indicates the $20\,m\,s^{-1}$ phase speed. The WRF control simulation captures the westward-propagating and diurnally oscillating rain rates observed in TRMM (Fig. 4, top two panels), although of smaller amplitude and lagged in time. The diurnal cycle of precipitation in the Panama Bight for the WRF control simulation shares a similar gravity wave propagation speed to that of TRMM, which is also confirmed by comparing high-pass-filtered vorticity and divergence anomalies between the model and ERA-Interim in the region (not shown). In observations, the most intense rain rates peak near 0700 local time just off the western coast, while in the WRF control simulation the most intense rain rates are delayed by about 6 h in the same area. Similar to these results, the regional modeling simulation used to analyze the diurnal patterns of rainfall in northwest South America by Warner et al. (2003) also underestimated the amplitude of the precipitation rates in the Panama Bight while still capturing the overall pattern and mechanism of diurnal rainfall. Importantly, both TRMM and the WRF control simulation routinely produce diurnal precipitation anomalies to the west of 80°W. Mesoscale convective systems in WRF associated with high-frequency and synoptic variability tend to amplify along the Pacific coast of Central America, as suggested by comparing Figs. 3 and 4. In the WRF modified topography simulation, composite diurnal precipitation rates are dramatically reduced in the EPAC when compared to the control simulation and TRMM (Fig. 4, bottom). There is no evidence of systematic precipitation propagation in the WRF modified topography simulation.

The WRF control simulation shows westward-propagating synoptic variability in the EPAC with amplitude comparable to or higher than observations, as can be seen in a plot of 550-hPa relative vorticity averaged from 3° to 11°N during the summer of 2008 (Fig. 5, top). Synoptic waves with similar durations and locations of initiation are easily seen when comparing the control simulation and ERA-Interim (see Figs. 8, 9), although the precise timing of strong EW periods does not necessarily agree. The synoptic waves in the WRF control simulation are generally stronger than those in ERA-Interim. Similar behavior is consistently observed when comparing other summer seasons. A contributing factor to the greater intensification of EWs in the WRF control simulation may be that the waves are associated with much stronger convective anomalies than in observations (see Figs. 8, 9), especially near the coasts of Central America and Mexico. The downstream development of EWs over Africa has been strongly linked to the intensity of upstream convective anomalies (Thorncroft et al. 2008). In the WRF control simulation, convective anomalies associated with developing EWs are stronger earlier in the life cycle than in observations, possibly leading to a quicker intensification and greater amplitude than the observed disturbances.

Relative vorticity, averaged from 3° to 11°N for the modified topography simulation, is shown in the bottom panel of Fig. 5. When local rainfall variability near the Panama Bight is suppressed, EW and TC activity in the EPAC is reduced in amplitude and regularity, suggesting that high-frequency convective variability is important to the initiation and maintenance of most EPAC EWs. The remaining EWs appear to be associated with preexisting disturbances entering from the Caribbean, as can be seen most prominently around 1 July and 1 October. These results are consistent with the other summer seasons (not shown). A more general comparison of EW variance between the control and modified topography simulation is shown below.

The relationship of EPAC EWs to those in the Caribbean is further examined by performing a lag correlation of 2.5–12-day bandpass-filtered 550-hPa vorticity anomalies between the EPAC and Caribbean over all summer seasons (Fig. 6). The filtered vorticity anomalies

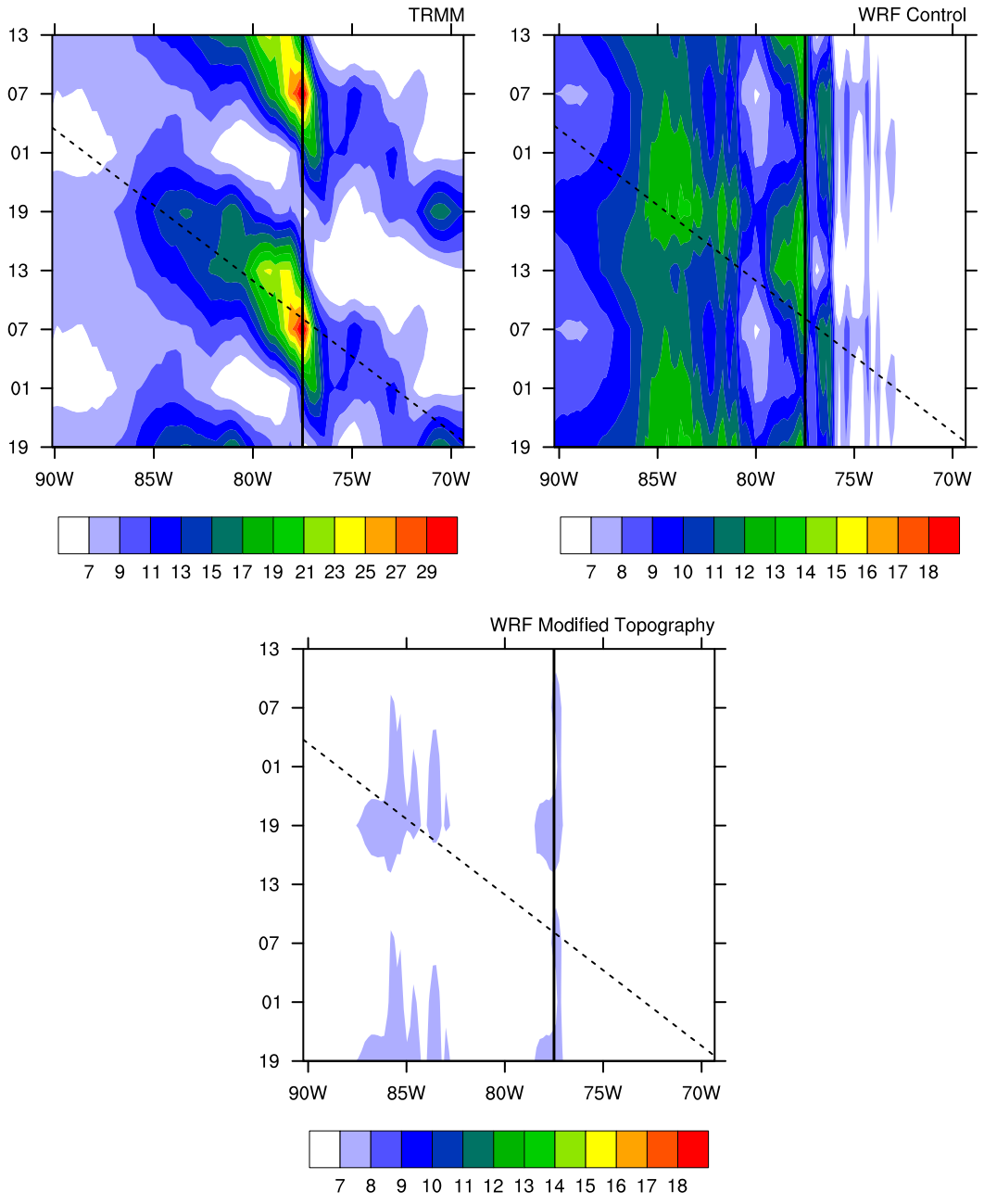

FIG. 4. Local time–longitude sections of precipitation rate (mm day^{-1}) composited for each 6-h time step and averaged from 3° to 11°N for the (top left) TRMM observations, (top right) WRF control simulation, and (bottom) WRF modified topography simulation. Solid black line indicates Pacific coast of South America. Dashed line indicates a phase speed of 20 m s^{-1}. The plots are repeated in time for clarity.

are averaged over 5° × 5° boxes centered at 9°N, 87°W in the EPAC and 9°N, 64.5°W in the Caribbean. The results are not sensitive to reasonable changes in the longitude but are sensitive to changes in latitude, particularly when only one of the averaging boxes is moved north or south. Statistical significance is calculated using the two-tailed t test with a p value of 0.05. In the control simulation, modest, but significant, positive correlations peak at −2.25 days, when EW vorticity in the Caribbean leads that in the EPAC. Significant positive correlations are present in the modified topography simulation between lags −2 and −3 days. These correlations are approximately twice the value of those occurring at similar lags in the control simulation and also larger than those

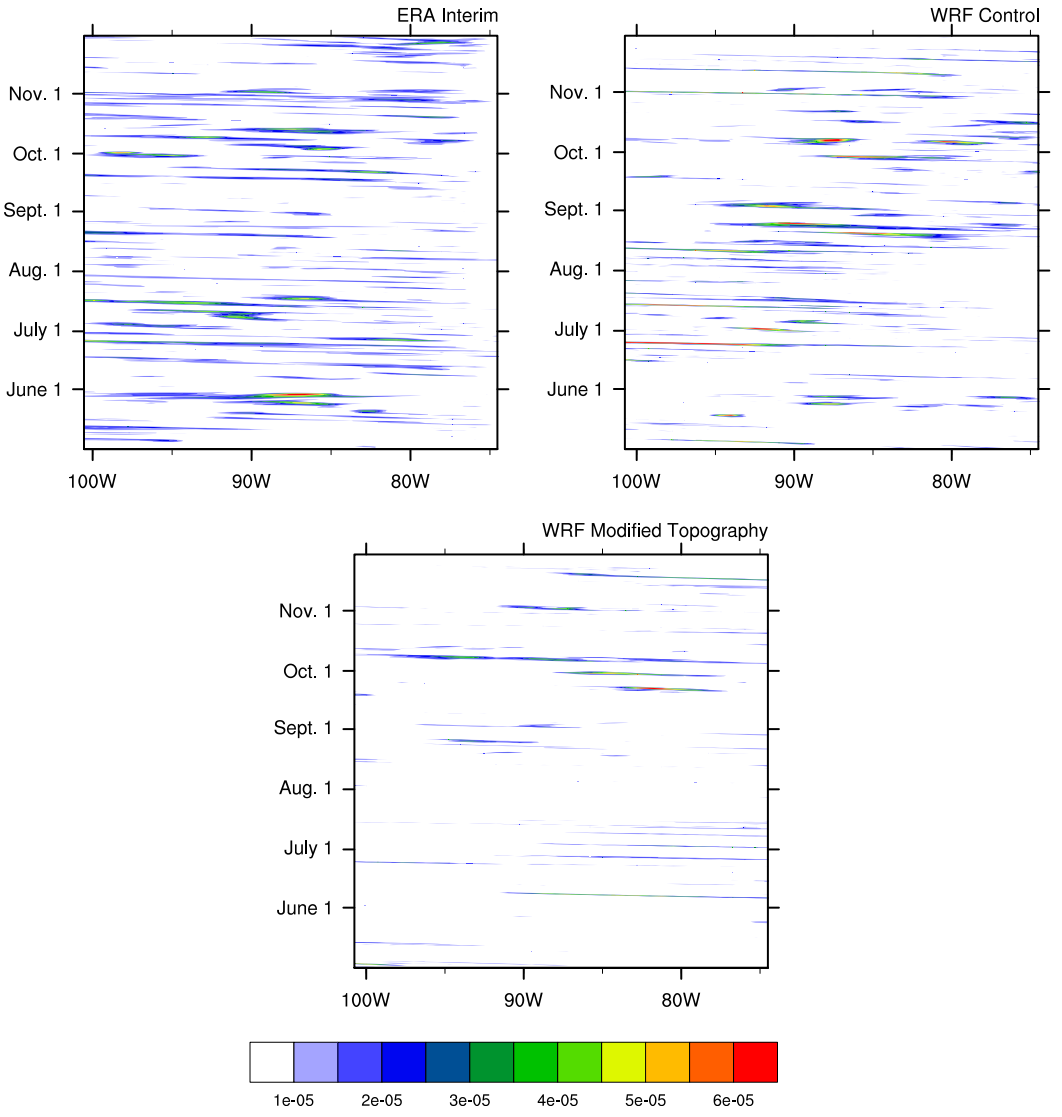

FIG. 5. The 550-hPa relative vorticity averaged from 3° to 11°N is shown as a function of time vs longitude for (top left) ERA-Interim, (top right) WRF control, and (bottom) WRF modified topography for May–November 2008. Vorticity in all WRF simulations has been interpolated to the same grid as ERA-Interim.

in observations. This suggests that EWs in the Caribbean are responsible for forcing EWs in the EPAC to a greater degree when convective variability near the Panama Bight is suppressed, although correlations remain modest. The greater ability of low-level signals to cross Central America without being blocked may also contribute to the higher correlation in the modified topography experiment.

The reduction in EW variability in the WRF modified topography simulation compared to the control simulation is further confirmed by examining the 2.5–12-day bandpass-filtered relative vorticity variance at 550 hPa (Fig. 7, middle and bottom panels). In both the ERA-Interim and WRF control simulation, a trail of vorticity variance leads from the Panama Bight to the northwest, although the variance is much stronger in the control simulation through much of the EPAC warm pool. Filtered vorticity variance in the modified topography simulation is significantly reduced over most of the EPAC EW track compared to that of the control simulation. The contour scale is logarithmic and indicates that filtered vorticity variance is reduced by approximately half in the regions of maximum variance near 15°N, 105°W when comparing the control and modified topography simulations.

The sensitivity tests using WRF support the idea that both EWs propagating from West Africa and those initiated locally, associated with strong convective

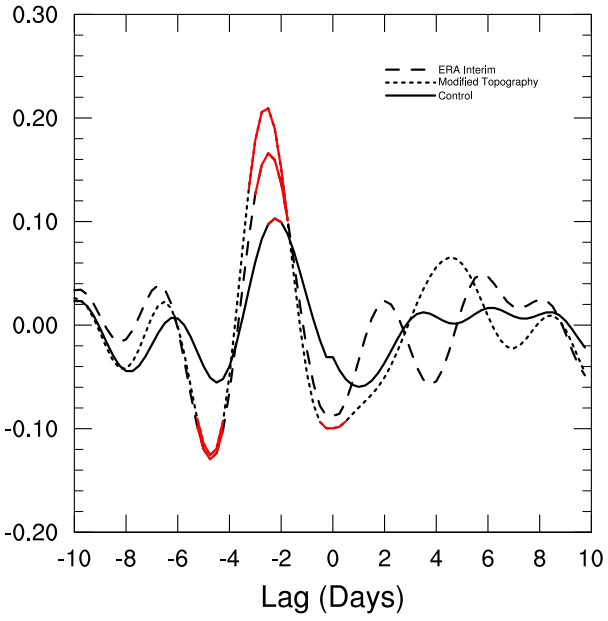

FIG. 6. Lag correlation of 2.5–12-day bandpass-filtered vorticity at 550 hPa between 5° × 5° boxes centered in the east Pacific at 9°N, 87°W and in the Caribbean at 9°N, 64.5°W for ERA-Interim (dashed), WRF modified topography (dotted), and WRF control (solid) is shown. Red lines indicate correlations that are significant at the 95% confidence threshold. Negative lags indicate periods when EW vorticity in the Caribbean leads that in the EPAC.

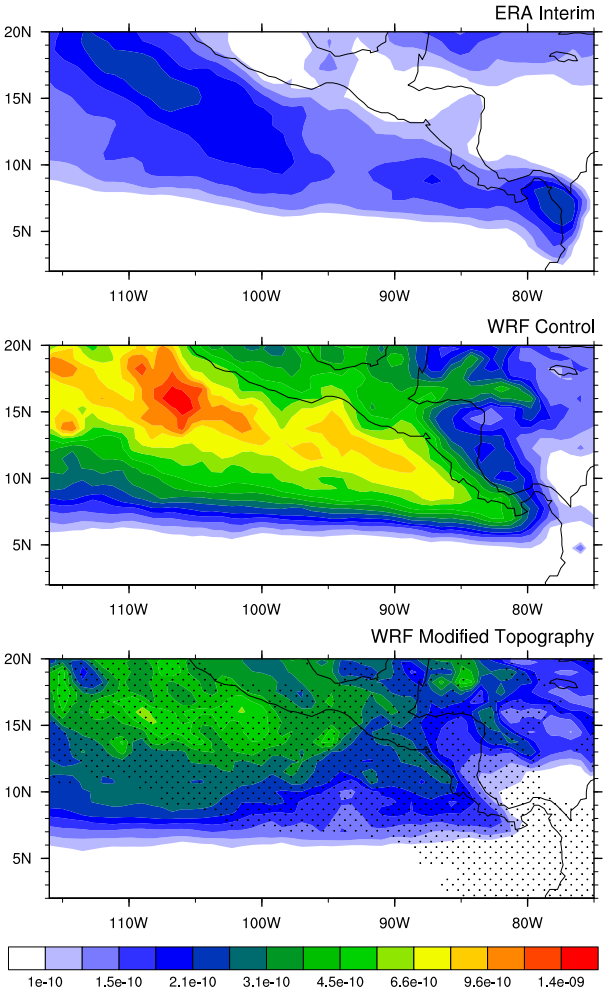

FIG. 7. The 2.5–12-day bandpass-filtered 550-hPa relative vorticity variance (s^{-2}; color contours) is shown for (top) ERA-Interim, (middle) WRF control, and (bottom) WRF modified topography for May–November 2000–09. Stippling in the WRF modified topography indicates variance values that reject the null hypothesis that they are of the same population as the WRF control at the 95% confidence level using the two-tailed *f* test. Vorticity in WRF simulations has been interpolated to the same grid as ERA-Interim.

pulses in the Panama Bight, are important to the number and intensity of EWs in the EPAC. An additional simulation was performed in which EWs were filtered from the lateral boundary forcing of WRF. Specifically, winds, temperature, geopotential height, and moisture were removed in the wavenumber–frequency space typically occupied by EWs. Using the filtered boundary forcing, EW variability is significantly reduced but not to the same degree as observed in the WRF modified topography simulation, suggesting that vigorous synoptic variability can be generated even in the absence of remote forcing. The results of this simulation are not emphasized here because of concerns about the poor mean state, particularly an unrealistic Caribbean low-level jet. The next section examines the process by which EW vorticity organizes and grows during the early stages of EPAC EW development.

4. Easterly wave initiation and amplification

Synoptic vorticity variance is significantly reduced across the EPAC in WRF when high-frequency convective variability near the Panama Bight is suppressed. In this section, we investigate mechanisms through which strong transient disturbances emerging from the Panama Bight are able to initiate and amplify EW vorticity anomalies. Because predecessor vorticity at midlevels is theorized to be critical to the genesis of tropical cyclones in the EPAC and elsewhere (e.g., Bister and Emanuel 1997; Raymond et al. 1998; Nolan 2007; Davis and Ahijevych 2013; Raymond et al. 2014; Davis 2015), we are interested in the processes responsible for the origination and development of midlevel vorticity anomalies that characterize EWs. To examine the evolution of the vorticity field associated with EWs, lag composites of EWs are shown. The composites are based on a local index of standardized 2.5–12-day bandpass-filtered 550-hPa vorticity anomalies averaged over a 5° × 5° box centered off the coast of Costa Rica (9°N, 87°W). [Note that significant

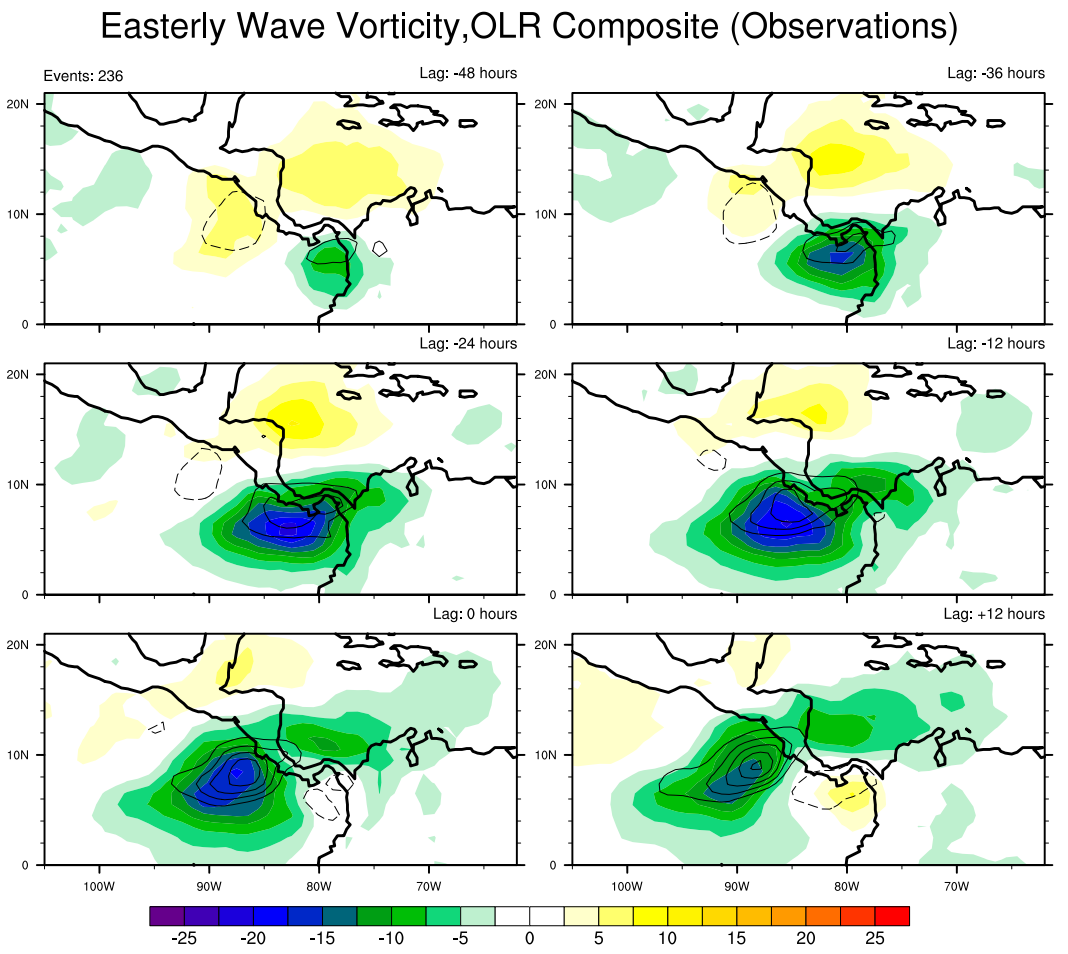

FIG. 8. Lag composites of 550-hPa relative vorticity (line contours) and OLR (shading; W m^{-2}) anomalies defined as deviations from a 10-day running mean for ERA-Interim are shown. Vorticity contour interval is 5×10^{-6} s^{-1}. Negative (positive) contours are solid (dashed), and the zero contour is omitted. The number of EW events in the composites is shown in the upper-left corner.

power in the model and ERA-Interim is observed at EW periods for meridional winds averaged over the 5° × 5° box (not shown).] Local maxima greater than 1.0 standard deviation in the index are defined as EW events. Lag composites are then generated relative to the peak of the index at lag 0. The general evolution of the vorticity composites is not sensitive to reasonable variations in the box size, location, or index threshold.

Figure 8 shows the EW composites as a function of lag for ERA-Interim 550-hPa vorticity and NCDC OLR anomalies defined as deviations from a 10-day running mean. This calculation of anomalies includes those at EW and higher-frequency time scales in order to better document the transition of strong Panama Bight disturbances into downstream EWs. Two days prior to the maximum vorticity anomaly amplitude off the coast of Costa Rica, vorticity anomalies at 550 hPa maximize off the northwest coast of Colombia, the same region where strong orographically generated diurnal rainfall pulses are well known to occur (i.e., Mapes et al. 2003a). This maximum strengthens and elongates westward off the south coast of Panama 12 h later. At lag −24 h, vorticity remains anchored on its eastern edge near the Panama Bight, leading to a broad east–west-oriented envelope of vorticity extending from the northwest coast of Colombia to the west coast of Costa Rica. At lag −12 h, the vorticity maximum is present in the EPAC with a one-half wavelength of ~1400 km, suggesting a complete wavelength of ~2800 km that is comparable to EWs observed in the EPAC using other EW compositing methods (i.e., Serra et al. 2008, 2010; Crosbie and Serra 2014; Rydbeck and Maloney 2014, 2015). At the peak of the event and the following 12 h, the vorticity maximum develops a southwest-to-northeast horizontal tilt and propagates to the northwest. In conjunction with the tilt of the wave, OLR anomalies are favored in the

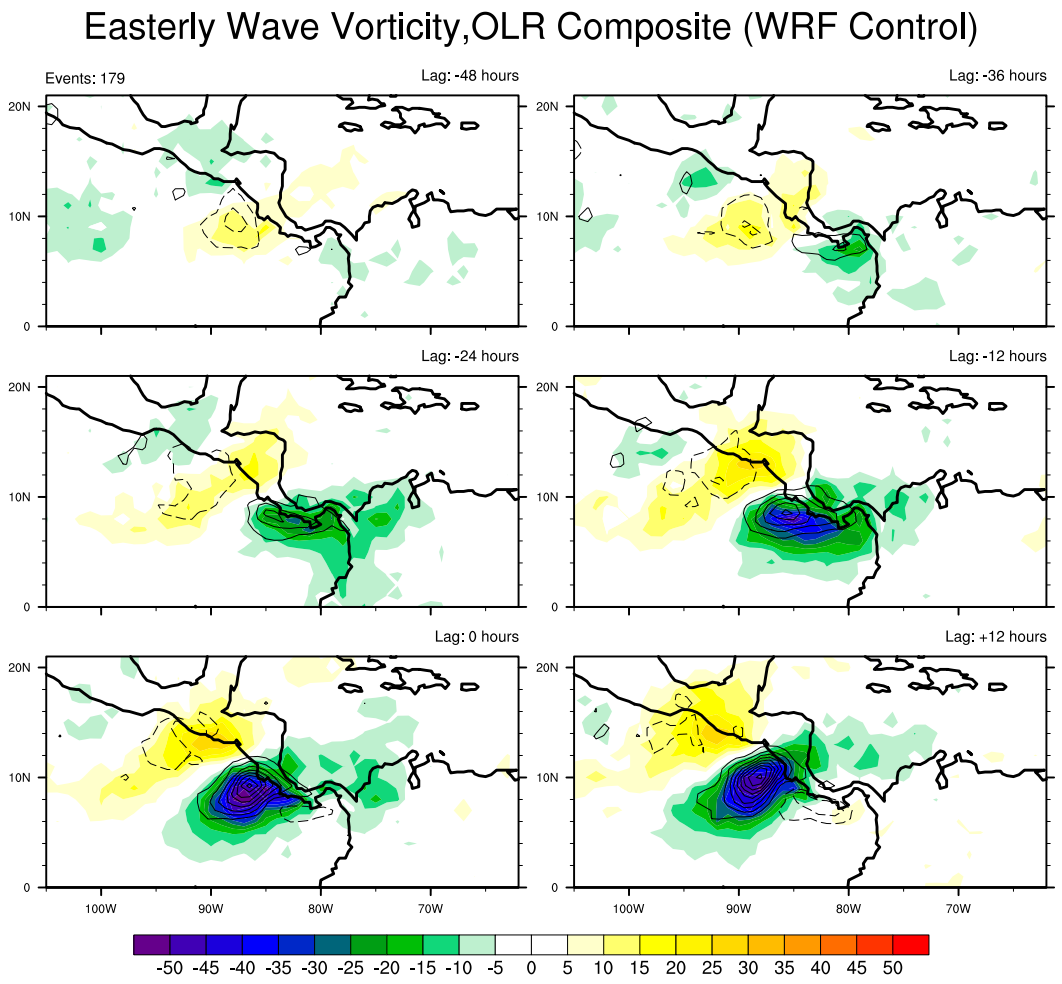

FIG. 9. Lag composites of 550-hPa relative vorticity (line contours) and OLR (shading; W m^{-2}) anomalies defined as deviations from a 10-day running mean for the WRF control simulation are shown. The vorticity contour interval is 7.5 $\times$ 10^{-6} s^{-1}. Negative (positive) contours are solid (dashed), and the zero contour is omitted. The number of EW events in the composites is shown in the upper-left corner.

southwest quadrant of the wave. Both the tilt and propagation direction of the vorticity anomalies are analogous to EW evolution in the EPAC, as shown in previous studies (i.e., Serra et al. 2008, 2010; Crosbie and Serra 2014; Rydbeck and Maloney 2014, 2015).

The same methodology is employed to produce lag composites of 550-hPa vorticity and OLR anomalies for the WRF control simulation (Fig. 9). Between lag −48 and −36 h, a weak local vorticity maximum and OLR minimum develop in the Panama Bight. The vorticity anomaly intensifies and zonally broadens while migrating westward between lag −36 and −12 h as the negative OLR anomalies intensify, like the evolution of anomalies in observations. At lag 0 h, a robust vorticity maximum with a southwest-to-northeast-tilted structure is developed off the coast of Central America. Similar to NCDC observations, the OLR minimum in WRF is predominantly positioned in the southwest quadrant of the wave. By lag +12 h, the wave has propagated to the west-northwest as anticyclonic vorticity anomalies have developed and intensified behind the EW. In general, the evolution of midlevel vorticity and OLR anomalies in the WRF control simulation broadly resembles the composites observed using ERA-Interim and NCDC data, suggesting that important features of the EWs are sufficiently represented in the model. However, the EW disturbances in WRF have higher amplitudes and are more compact (note the difference in shading and contour intervals on Figs. 8 and 9). At lags −48, −36, and −24 h, the observed westward-propagating OLR maximum in the Caribbean is considerably weaker in WRF. The Caribbean OLR maximum is perhaps related to phase shifts of select easterly waves propagating across Central America, as

observed in Toma and Webster (2010a). Lag composites of OLR and vorticity for the WRF modified topography simulation are much noisier and weaker than the WRF control simulation and ERA-Interim composites at all lags. Because of the difficulty in identifying coherently propagating features, the WRF modified topography composite is now shown. Next, the contribution of convective disturbances originating near the Panama Bight to the EW vorticity budget is investigated using output from the WRF control simulation.

a. Easterly wave vorticity balance

Rydbeck and Maloney (2015) previously looked at the vertically integrated vertical vorticity budget of the lower troposphere for EPAC EWs using ERA-Interim data and found that the most important contributions to the local change of EW vorticity were horizontal advection and vertical stretching. The present vorticity budget expands on that analysis to more specifically examine EWs in their formative stages and the importance of convective variability near the Panama Bight to the wave's vorticity tendency in WRF. The vertical vorticity tendency at a particular pressure level may be expressed as follows:

$$\left(\frac{\partial \zeta}{\partial t}\right)_{\mathrm{EW}} = -(V \cdot \nabla \eta)_{\mathrm{EW}} + \left(\eta \frac{\partial \omega}{\partial p}\right)_{\mathrm{EW}} + [\nabla \cdot (\zeta_h \omega)]_{\mathrm{EW}} + R, \quad (1)$$

where η is the absolute vorticity, $\partial\omega/\partial p$ is the divergence, ζ is the vertical relative vorticity, ζ_h is the horizontal relative vorticity, and the subscript "EW" represents 2.5–12-day bandpass-filtered terms. The term on the left-hand side (LHS) of Eq. (1) represents the local time rate of change of the vertical component of EW vorticity. The local change of EW vorticity results from horizontal advection and the effects of stretching and tilting, respectively, on the right-hand side (RHS). The residual R is calculated as the difference between the vorticity tendency on the LHS and the sum of the first three terms on the RHS. Contributions to the residual include processes not represented in the terms on the RHS, such as the effects of cumulus convection, other subgrid-scale processes, and friction. The residual term also includes any calculation errors in the terms comprising the budget. All variables are interpolated to a 1.5° × 1.5° grid before budget terms are calculated.

b. Easterly wave vorticity tendency

Composites of EW vorticity tendency and 2.5–12-day bandpass-filtered vorticity anomalies at 550 hPa are shown in Fig. 10. All composites shown in the vorticity analysis are based on the same EW index used in Fig. 9. We are interested in the processes occurring during the early "spinup" stages of EWs, so composites of terms in the vorticity budget are shown for lags −36, −12, and 0 h. At lag −36 h, a weak vorticity maximum is present in the Panama Bight with a vorticity tendency maximum that is 90° out of phase to the west-northwest of the EW vorticity maximum, although a positive vorticity tendency exists coincident with the vorticity center. East of the wave axis, near the coast of South America, the vorticity tendency is weak and below the contour color scale. Hence, positive vorticity preferentially grows near and to the west of the region of enhanced vorticity. By lag −12 h, the EW has become zonally elongated,

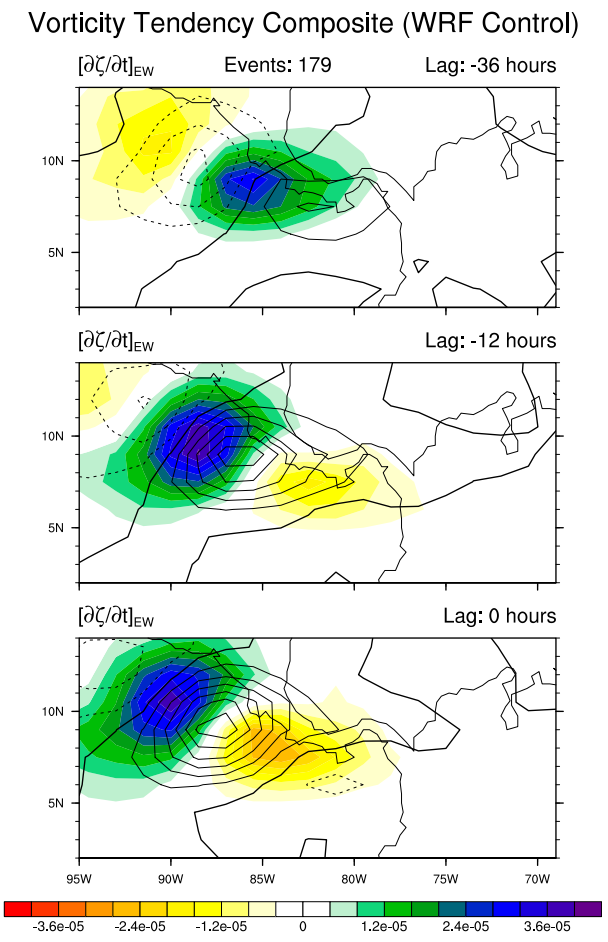

FIG. 10. Lag composites of 2.5–12-day bandpass-filtered 550-hPa relative vorticity anomalies (s^{-1}; line contours) and 2.5–12-day bandpass-filtered vorticity tendency ($s^{-1}\,day^{-1}$; color contours) for the WRF control are shown. Vorticity contour interval is $5 \times 10^{-6}\,s^{-1}$. The thick solid line is the zero vorticity contour. The number of EW events in the composites is shown above the panels.

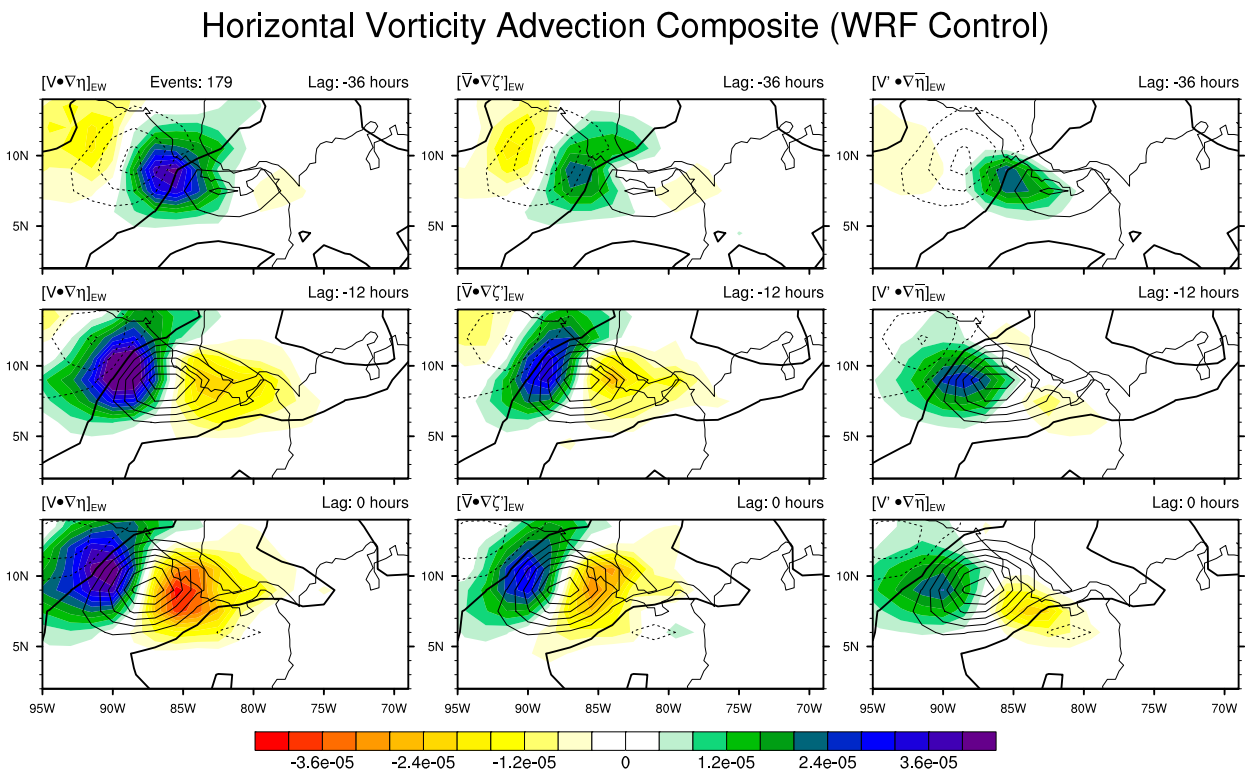

FIG. 11. Lag composites of 2.5–12-day bandpass-filtered 550-hPa relative vorticity anomalies (s^{-1}; line contours) and 2.5–12-day bandpass-filtered (left) vorticity advection anomalies (s^{-1} day^{-1}; color contours), (middle) relative vorticity anomalies advected by the mean wind, and (right) mean absolute vorticity anomalies advected by the wind anomalies for the WRF control are shown. Vorticity contour interval is 5×10^{-6} s^{-1}. The thick solid line is the zero vorticity contour. The number of EW events in the composites is shown in the upper-left corner.

resulting from the leading edge being propagated to the west-northwest while the trailing edge of the EW is propagated in the same direction much more slowly. The vorticity tendency maximum is 1/8 wavelength ahead of the vorticity maximum at lag −12 h, suggesting that the disturbance is both intensifying and propagating. The vorticity tendency minimum to the east is only 35%–45% of the magnitude of the tendency maximum to the west, thus enhancing the zonally elongated structure of the wave. By lag 0 h, the vorticity tendency minimum has intensified to 65%–75% of the magnitude of the tendency maximum, largely halting the zonal elongation of the EW observed at earlier lags. Next, terms on the RHS of Eq. (1) that set the zonal wavelength of the EW and contribute to its growth are assessed.

c. *Easterly wave vorticity advection*

The horizontal advection of vorticity is shown in Fig. 11 (left column). The advection is of comparable magnitude and mostly collocated with the vorticity tendency, suggesting that the majority of the vorticity tendency is due to advection, similar to what is found in observations (Rydbeck and Maloney 2015). The advection maximum is in quadrature with the EW vorticity field at lag −36 h but is between 1/4 and 1/8 wavelength ahead of the maximum at lags −12 and 0 h. Although it is difficult to see the precise phasing of the advection in Fig. 11 (left column), the phasing was confirmed using a different plotting scale and is apparent when analyzing the components of the advection term discussed later (Fig. 11, middle and right columns). The advection minimum is 1/8 wavelength to the east of the EW vorticity maximum at lags −12 and 0 h. The ratio of magnitudes between the advection maximum to the west and minimum to the east at each lag is comparable to that of the tendency. This suggests that advection is the major contributor to the zonal elongation of EWs during their formative stages, helping to increase the EW zonal wavelength.

To further interpret this behavior, the horizontal advection term in the vorticity budget is linearly decomposed into variables consisting of 10-day running means (variables with overbars) and deviations from those 10-day running means (primed variables) such that the advection may be expressed as follows:

$$-(V\cdot\nabla\eta)_{\mathrm{EW}}\approx-(\overline{V}\cdot\nabla\zeta')_{\mathrm{EW}}-(V'\cdot\nabla\overline{\eta})_{\mathrm{EW}}-(V'\cdot\nabla\zeta')_{\mathrm{EW}}. \quad (2)$$

Thus, the horizontal advection of vorticity on the LHS of Eq. (2) is approximated as the sum of the mean winds acting on the anomalous relative vorticity gradient, the anomalous winds acting on the mean absolute vorticity gradient, and the anomalous winds acting on the anomalous relative vorticity gradient, respectively. The first two terms on the RHS of Eq. (2) are larger than the last term at each lag and describe the majority of the horizontal advection. The lag composites of the first term on the RHS of Eq. (2), $-(\overline{V}\cdot\nabla\zeta')_{\mathrm{EW}}$, are shown in Fig. 11 (middle column). The mean wind acting on the anomalous vorticity gradient strongly mirrors the total advection term and is the largest of the three terms on the RHS of Eq. (2). This suggests that EPAC EWs are predominantly advected by the mean flow. The effect of the anomalous wind acting on the mean absolute vorticity gradient has a similar structure but is slightly weaker in amplitude at lags −12 and 0 h (Fig. 11, right column). A positive contribution of this term to the vorticity center is evident at lags −36 and −12 h resulting from the advection of mean relative vorticity by the anomalous winds. The anomalous winds are advecting along a strong meridional gradient that results from a reservoir of maximum mean relative vorticity to the north of the anomalous vorticity center [see Fig. 12 of Rydbeck and Maloney (2014)]. Although not shown, the anomalous advection of mean relative vorticity is 2–4 times greater in magnitude than the beta advection prior to lag 0. The last term on the RHS of Eq. (2), $-(V'\cdot\nabla\zeta')_{\mathrm{EW}}$, opposes the west-northwestward propagation and intensification of the wave with minima below $-1.5\times10^{-5}\,\mathrm{s^{-1}\,day^{-1}}$ (not shown), consequently reducing the net effect of the other two terms.

d. Easterly wave vorticity stretching

The vorticity stretching term [second term on the RHS of Eq. (1)] is shown in Fig. 12. Stretching is the largest term in the vorticity budget composite at lag 0 and is approximately 1/8 wavelength behind the EW, leading to an amplification in EW intensity but a reduction in westward phase speed. The stretching anomaly on the east side of the disturbance contributes to the zonal elongation of the wave, thus increasing the EW's zonal wavelength. The positive vorticity tendency due to stretching on the east side of the wave counters the negative vorticity tendency there due to advection (Fig. 11, left column).

Important to the stretching term of the vorticity budget is the nature of the convective heating in these disturbances that drives horizontal convergences of vorticity. Figure 13 shows the 10-day high-pass-filtered apparent heat source (Q1) profile averaged over a 5° × 5° box that is centered on the 550-hPa vorticity maximum and averaged over the formative phase of the EW life cycle, specifically lags −48, −36, and −24 h. The vertical profile of Q1 during the incipient stages of the easterly wave life cycle in the model is a combination of stratiform and deep convective heating that maximizes at 400 hPa with a value of ~1.6 K day^{-1}. Composited over the same lags, a similar Q1 profile is also evident in ERA-Interim data, although the peak at 400 hPa is roughly half the magnitude of that in the control simulation. Midlevel convergence inferred from the heating profile in Fig. 13 supports the patterns of vorticity stretching discussed above. Similar to the results shown here, Zuluaga and Houze (2015) show using TRMM

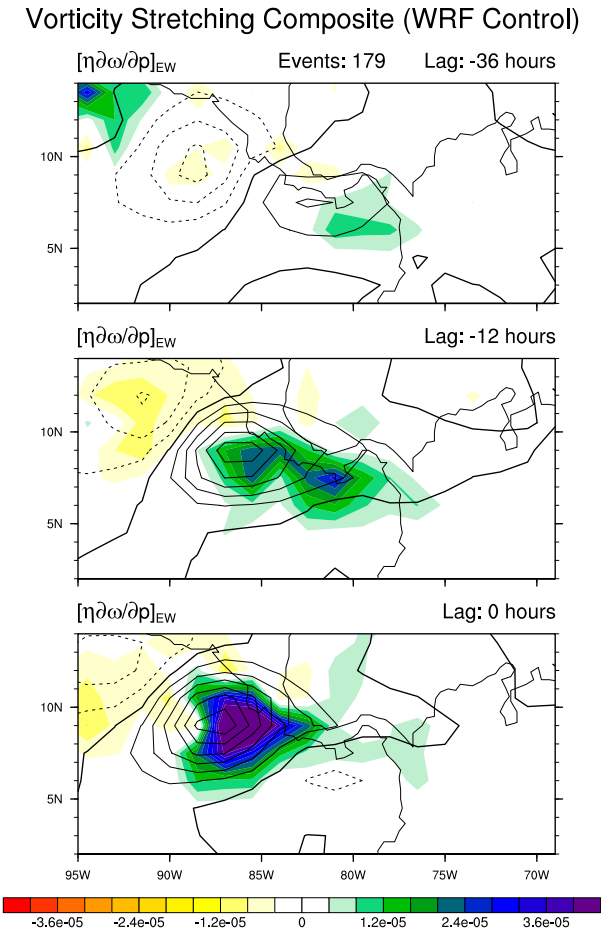

FIG. 12. Lag composites of 2.5–12-day bandpass-filtered 550-hPa relative vorticity anomalies ($\mathrm{s^{-1}}$; line contours) and 2.5–12-day bandpass-filtered vorticity stretching anomalies ($\mathrm{s^{-1}\,day^{-1}}$; color contours). Vorticity contour interval is $5\times10^{-6}\,\mathrm{s^{-1}}$. The thick solid line is the zero vorticity contour. The number of EW events in the composites is shown above the panels.

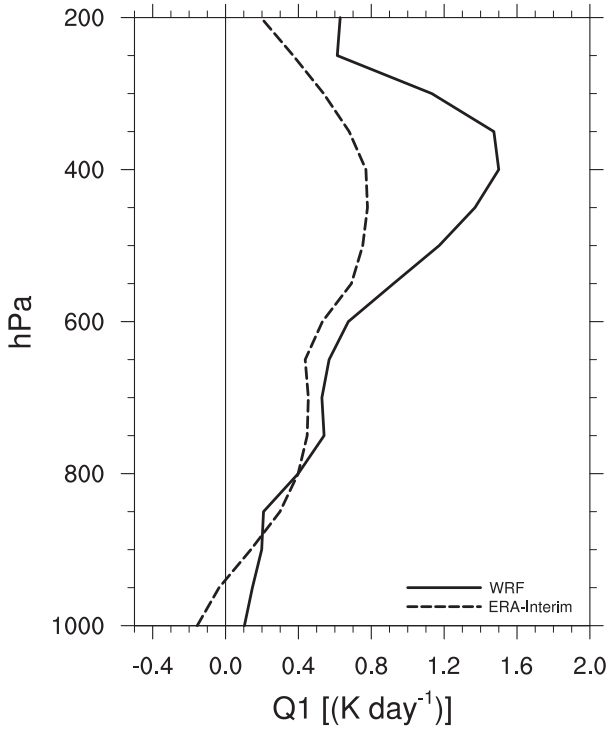

FIG. 13. Lag composites of 10-day high-pass-filtered Q1 profile ($K\,day^{-1}$) for the WRF control simulation (solid) and ERA-Interim (dashed) are averaged over lags −48, −36, and −24 h. Heating rates are averaged over a 5° × 5° box centered on the 550-hPa vorticity maximum at each lag.

observations that broad stratiform regions routinely form and are associated with strong midlevel convergence anomalies just off the Pacific coastline of South America.

To further explore the roles of vorticity and divergence anomalies at various time scales to EW vorticity generation, the stretching term is partitioned into 10-day running-mean variables and deviations from the 10-day running mean, as in Eq. (2), and written as

$$\left(\eta\frac{\partial\omega}{\partial p}\right)_{\mathrm{EW}} \approx \left(\overline{\eta}\frac{\partial\omega'}{\partial p}\right)_{\mathrm{EW}} + \left(\zeta'\frac{\partial\overline{\omega}}{\partial p}\right)_{\mathrm{EW}} + \left(\zeta'\frac{\partial\omega'}{\partial p}\right)_{\mathrm{EW}}. \tag{3}$$

The first two terms on the RHS of Eq. (3) are shown in Fig. 14 (middle and right columns, respectively). The anomalous stretching of the mean absolute vorticity, $(\overline{\eta}\partial\omega'/\partial p)_{\mathrm{EW}}$, is positive 1/8 wavelength behind the EW vorticity maximum at lags −12 and 0 h, similar to the total stretching term. The maxima of the anomalous stretching of the mean absolute vorticity are collocated with regions where the mean vorticity maxima in the monsoon trough overlaps regions of anomalous horizontal convergence at and to the east of the EW axis (not shown). Maxima of the stretching of anomalous vorticity by the mean divergence, $(\zeta'\partial\overline{\omega}/\partial p)_{\mathrm{EW}}$, (Fig. 12, right column) slightly lag the EW vorticity maximum, contributing to the intensification and slowing of the west-northwestward propagation of the EW. Because both of these linearized stretching terms oppose the west-northwestward propagation of the EW predominantly on the wave's eastern flank, the terms increase the zonal wavelength of the wave by zonally elongating the vorticity field. The last term on the RHS of Eq. (3), $(\zeta'\partial\omega'/\partial p)_{\mathrm{EW}}$, is shown in the left column of Fig. 14. This anomalous stretching term is the strongest of all the vorticity stretching components on the RHS of Eq. (3). Similar to the total stretching term, the maximum of $(\zeta'\partial\omega'/\partial p)_{\mathrm{EW}}$ lags the EW vorticity maximum by approximately 1/8 wavelength, thus reinforcing the patterns and effects of the first two terms on the RHS of Eq. (3).

e. *Easterly wave vorticity tilting and residual*

The tilting term in Eq. (2) is much weaker than the stretching and horizontal advection terms but does contribute to the zonal elongation of the wave during lags −36, −12, and 0 h (not shown) with maximum values from 0.8×10^{-6} to $2.4 \times 10^{-6}\,s^{-1}\,day^{-1}$. The positive maxima in the tilting term are confined to regions over land and do not continuously propagate with the EW as observed in the advection and stretching terms of the vorticity budget. This suggests that sea-breeze-type convection and/or the mechanical tilting effects of the terrain in Central America might be important.

Figure 15 shows the sum of grid-scale stretching, grid-scale tilting, and the residual that includes subgrid-scale effects for lags −36, −12, and 0 h. The sum of terms shown in Fig. 15 is largely collocated with maxima of midlevel vertical velocity anomalies, suggesting that the net vorticity tendency resulting from stretching, tilting, and the residual is strongly determined by convection in the model. While the broad pattern in Fig. 15 shows many similarities to the stretching term in Fig. 12 and indicates a strong influence from stretching, there are some interesting differences regarding the precise spatial location that might influence the dynamics of the waves. At lag −36 h, the net effect of the combined residual is to elongate the wave to the east and oppose the tendency by horizontal advection to the west of the wave. At lags −12 and 0 h, the combined residual affects a positive vorticity tendency in the northeast quadrant of the EW vorticity maximum. This pattern of vorticity tendency leads to a southwest-to-northeast horizontal tilt of the wave that is favorable for barotropic conversions that lead to increased EW kinetic energy, consistent with the results of Rydbeck and Maloney (2015). Supplementary information

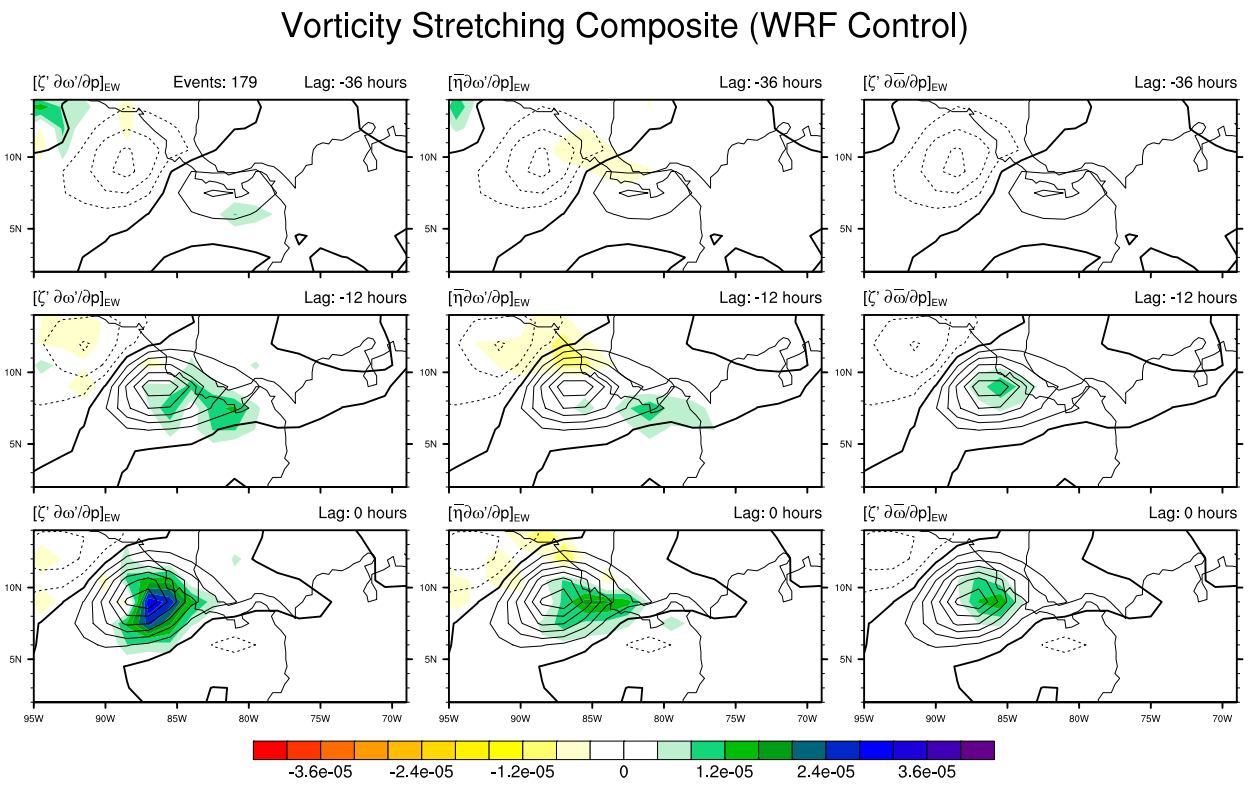

FIG. 14. Lag composites of 2.5–12-day bandpass-filtered 550-hPa relative vorticity anomalies (s^{-1}; line contours) and (left) 2.5–12-day bandpass-filtered vorticity stretching of anomalous vorticity by the anomalous divergence (s^{-1} day^{-1}; color contours), (middle) 2.5–12-day bandpass-filtered stretching of mean absolute vorticity by the anomalous divergence, and (right) 2.5–12-day bandpass-filtered stretching of relative vorticity anomalies by the mean divergence for the WRF control are shown. Vorticity contour interval is 5×10^{-6} s^{-1}. The thick solid line is the zero vorticity contour. The number of EW events in the composites is shown in the upper-left corner.

regarding the vorticity balance and secondary terms can be found in Rydbeck and Maloney (2015).

5. Discussion and conclusions

Many previous studies have suggested that the majority of EPAC EWs form in association with preexisting EWs propagating from West Africa. Obvious cases exist in which robust EWs with considerable convection are able to propagate from West Africa and across the Caribbean with strong signatures in satellite imagery. However, EWs routinely weaken over the western Atlantic and Caribbean, regions of strong EW lysis. Thus, understanding mechanisms of EW formation and/or reinvigoration are critical to forecasting EPAC EWs and the TCs into which they may develop.

The sensitivity of EPAC EWs to a hypothesized mechanism of local forcing is investigated in WRF. Two simulations are analyzed in this study: a control simulation and a modified topography simulation. In the modified topography simulation, westward-propagating convective variance in the Panama Bight is suppressed by reducing the model terrain height in northern South America and portions of Central America. Under these conditions, EPAC EW variance is significantly reduced in the EPAC warm pool. The significant reduction in EW variance by suppressing convective variability in and around the Panama Bight in WRF indicates that mechanisms of EW formation and intensification are likewise suppressed. In this modified topography simulation, extant EPAC EWs increase their correlation with EWs in the Caribbean at 2–3-day leads relative to a control simulation, suggesting a stronger relationship to Atlantic EWs when local forcing mechanisms are suppressed. In WRF, both remote forcing and local forcing mechanisms of EWs appear important to the distribution and amplitude of EPAC EWs.

In a separate simulation not shown in the analysis, EWs propagating from Africa are removed from the lateral boundary forcing of WRF. This is accomplished by filtering winds, temperature, moisture, and geopotential height to remove westward-propagating, synoptic-scale variability at all vertical levels. Under these conditions, EW variance in the EPAC warm pool is significantly reduced, although to a lesser degree than the modified topography simulation. This result affirms

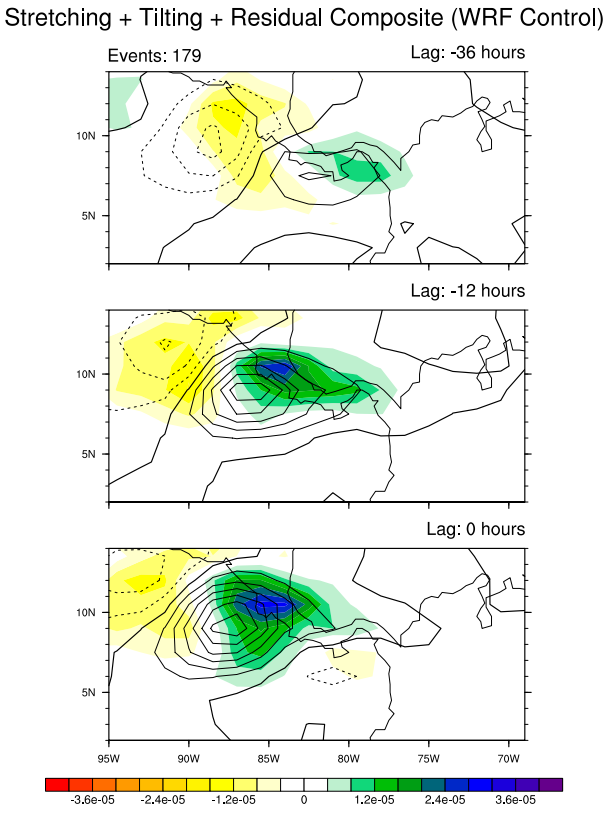

FIG. 15. Lag composites of the 2.5–12-day bandpass-filtered 550-hPa relative vorticity anomalies (s^{-1}; line contours) and sum of the 2.5–12-day bandpass-filtered stretching, tilting, and residual tendency (s^{-1} day^{-1}; color contours) for the WRF control are shown. Vorticity contour interval is 5×10^{-6} s^{-1}. The thick solid line is the zero vorticity contour. The number of EW events in the composites is shown above the panels.

the findings of the modified topography simulation, which suggests that both upstream EW variability and local mechanisms are important to the formation of EWs in the EPAC.

We further analyzed the processes by which local forcing is able to initiate and amplify EW vorticity anomalies. In the WRF control simulation, the local vorticity tendency during the formative stages of EWs is most strongly regulated by horizontal advection and stretching, similar to the findings of Rydbeck and Maloney (2015) using ERA-Interim. Horizontal advection of positive vorticity anomalies preferentially occurs on the western side of the growing vorticity disturbance, with weaker advection of negative vorticity anomalies occurring on the eastern side. The zonally unbalanced advection leads to a zonal elongation of the wave. Additionally, vertical stretching of vorticity anomalies largely occurs 1/8 wavelength to the east of the wave axis. Stretching to the east of the wave axis helps anchor vorticity anomalies there, further supporting the zonal elongation of the EW such that the EW zonal wavelength is increased. A partial collocation of stretching and advection of mean vorticity by the anomalous winds with the growing vorticity center helps to amplify the disturbance.

Partitioning of the vorticity budget indicates an important role for mesoscale convective systems near the Panama Bight in contributing to vorticity generation by stretching within growing EWs. We hypothesize that the convective systems generate seeds of EW vorticity that are necessary for further EW growth to take place. The vorticity seed is then able to grow into a robust EW in a matter of days via conversions from barotropic and perturbation available potential energy to perturbation kinetic energy (Rydbeck and Maloney 2014). The transition of mesoscale convective features to longer time scales has also been observed west of Sumatra and Borneo (Johnson and Ciesielski 2013) as well as Africa (Thorncroft et al. 2008), suggesting that analogous processes might occur elsewhere in the tropics. Verification of this process requires further modeling and observational analysis. The vorticity budget analysis distinguishes processes important to the horizontal-scale selection of EW vorticity in a localized region of the EPAC.

EPAC EWs are well known to be sensitive to variations in the background atmosphere, particularly on intraseasonal time scales. Rydbeck and Maloney (2015) note that the convective intensity in the Panama Bight remains largely unchanged when averaged over respective intraseasonal phases, suggesting that the seeding mechanism proposed herein might be resistant to variations of the background atmosphere. However, downstream growth of mesoscale convective systems might be affected by variations to the basic state. This requires further investigation. Related to this topic, accurate representation of the EPAC mean state across the model simulations is a limitation of this study. The model simulation in which convective variability near Central America is suppressed displays notable departures of the mean state from that of the control simulation. While changes to the mean state might be a result of suppressing EWs, we cannot rule out the alternative; changes to the mean state result in the suppression of EWs.

In this paper, we propose a mechanism of in situ EW generation and amplification that does not necessarily rely upon a continuous propagation of EWs from West Africa. In light of these results, mesoscale convective systems that lead to strong midlevel vorticity anomalies are hypothesized to function as nuclei for EPAC EW formation in the absence of any preexisting EWs entering the EPAC from the east. The effects of local convective activity on EW vorticity anomalies are not exclusive to EW formation but also apply to the

reenergizing of atrophied EWs propagating across the Caribbean Sea from West Africa. In this framework, better understanding and simulations of convective organization near the Central and South American coasts and their interactions with the background atmospheric state will enhance forecast skill of EPAC EWs.

Acknowledgments. The authors wish to thank Richard Johnson, Thomas Birner, and two anonymous reviewers for helpful comments and suggestions. We would like to acknowledge high-performance computing support from Yellowstone (ark:/85065/d7wd3xhc) provided by NCAR's Computational and Information Systems Laboratory, sponsored by the National Science Foundation. This work was supported by the NOAA Climate Program Office Modeling, Analysis, Predictions, and Projections under Contract NA12OAR4310077 and by the Climate and Large-Scale Dynamics Program of the National Science Foundation under Grant AGS-1347738. The statements, findings, conclusions, and recommendations do not necessarily reflect the views of NSF, NOAA, or the Department of Commerce.

REFERENCES

Aiyyer, A. R., and J. Molinari, 2008: MJO and tropical cyclogenesis in the Gulf of Mexico and eastern Pacific: Case study and idealized numerical modeling. *J. Atmos. Sci.*, **65**, 2691–2704, doi:10.1175/2007JAS2348.1.

Alaka, G. J., 2014: African easterly wave energetics on intraseasonal timescales. Ph.D. dissertation, Colorado State University, 214 pages.

Avila, L. A., and R. J. Pasch, 1992: Atlantic tropical systems of 1991. *Mon. Wea. Rev.*, **120**, 2688–2696, doi:10.1175/1520-0493(1992)120<2688:ATSO>2.0.CO;2.

——, and ——, 1995: Atlantic tropical systems of 1993. *Mon. Wea. Rev.*, **123**, 887–896, doi:10.1175/1520-0493(1995)123<0887:ATSO>2.0.CO;2.

Beven, J. L., L. A. Avila, J. L. Franklin, M. B. Lawrence, R. J. Pasch, and S. R. Stewart, 2005: Eastern North Pacific hurricane season of 2006. *Mon. Wea. Rev.*, **133**, 1403–1414, doi:10.1175/MWR2917.1.

Bister, M., and K. A. Emanuel, 1997: The genesis of Hurricane Guillermo: TEXMEX analyses and a modeling study. *Mon. Wea. Rev.*, **125**, 2662–2682, doi:10.1175/1520-0493(1997)125<2662:TGOHGT>2.0.CO;2.

Blake, E. S., and R. J. Pasch, 2010: Eastern North Pacific hurricane season of 2008. *Mon. Wea. Rev.*, **138**, 705–721, doi:10.1175/2009MWR3093.1.

——, and T. B. Kimberlain, 2013: Eastern North Pacific hurricane season of 2011. *Mon. Wea. Rev.*, **141**, 1397–1412, doi:10.1175/MWR-D-12-00192.1.

Chelton, D. B., M. H. Freilich, and S. K. Esbensen, 2000a: Satellite observations of the wind jets off the Pacific coast of Central America. Part I: Case studies and statistical characteristics. *Mon. Wea. Rev.*, **128**, 1993–2018, doi:10.1175/1520-0493(2000)128<1993:SOOTWJ>2.0.CO;2.

——, ——, and ——, 2000b: Satellite observations of the wind jets off the Pacific coast of Central America. Part II: Regional relationships and dynamical considerations. *Mon. Wea. Rev.*, **128**, 2019–2043, doi:10.1175/1520-0493(2000)128<2019:SOOTWJ>2.0.CO;2.

Collins, W. D., and Coauthors, 2004: Description of the NCAR Community Atmosphere Model (CAM 3.0). NCAR Tech. Note NCAR/TN-464+STR, 226 pp. [Available online at http://www.cesm.ucar.edu/models/atm-cam/docs/description/description.pdf.]

Crosbie, E., and Y. Serra, 2014: Intraseasonal modulation of synoptic-scale disturbances and tropical cyclone genesis in the eastern North Pacific. *J. Climate*, **27**, 5724–5745, doi:10.1175/JCLI-D-13-00399.1.

Davis, C. A., 2015: The formation of moist vortices and tropical cyclones in idealized simulations. *J. Atmos. Sci.*, **72**, 3499–3516, doi:10.1175/JAS-D-15-0027.1.

——, and D. A. Ahijevych, 2013: Thermodynamic environments of deep convection in Atlantic tropical disturbances. *J. Atmos. Sci.*, **70**, 1912–1928, doi:10.1175/JAS-D-12-0278.1.

Dee, D. P., and Coauthors, 2011: The ERA-Interim reanalysis: Configuration and performance of the data assimilation system. *Quart. J. Roy. Meteor. Soc.*, **137**, 553–597, doi:10.1002/qj.828.

Dunn, G. E., 1933: Tropical storms of 1933. *Mon. Wea. Rev.*, **61**, 362–363, doi:10.1175/1520-0493(1933)61<362:TSO>2.0.CO;2.

Ferreira, R. N., and W. H. Schubert, 1997: Barotropic aspects of ITCZ breakdown. *J. Atmos. Sci.*, **54**, 261–285, doi:10.1175/1520-0469(1997)054<0261:BAOIB>2.0.CO;2.

Frank, N. L., 1970: Atlantic tropical systems of 1969. *Mon. Wea. Rev.*, **98**, 307–314, doi:10.1175/1520-0493(1970)098<0307:ATSO>2.3.CO;2.

Hartmann, D. L., and E. D. Maloney, 2001: The Madden–Julian oscillation, barotropic dynamics, and North Pacific tropical cyclone formation. Part II: Stochastic barotropic modeling. *J. Atmos. Sci.*, **58**, 2559–2570, doi:10.1175/1520-0469(2001)058<2559:TMJOBD>2.0.CO;2.

Holton, J., J. Wallace, and J. Young, 1971: On boundary layer dynamics and the ITCZ. *J. Atmos. Sci.*, **28**, 275–280, doi:10.1175/1520-0469(1971)028<0275:OBLDAT>2.0.CO;2.

Hong, S.-Y., and J. O. J. Lim, 2006: The WRF single-moment 6-class microphysics scheme (WSM6). *J. Korean Meteor. Soc.*, **42**, 129–151.

——, Y. Noh, and J. Dudhia, 2006: A new vertical diffusion package with an explicit treatment of entrainment processes. *Mon. Wea. Rev.*, **134**, 2318–2341, doi:10.1175/MWR3199.1.

Jin, C. S., C. H. Ho, J. H. Kim, D. K. Lee, D. H. Cha, and S. W. Yeh, 2013: Critical role of northern off-equatorial sea surface temperature forcing associated with central Pacific El Niño in more frequent tropical cyclone movements toward East Asia. *J. Climate*, **26**, 2534–2545, doi:10.1175/JCLI-D-12-00287.1.

Johnson, R., and P. Ciesielski, 2013: Structure and properties of Madden–Julian oscillations deduced from DYNAMO sounding arrays. *J. Atmos. Sci.*, **70**, 3157–3179, doi:10.1175/JAS-D-13-065.1.

Kain, J. S., 2004: The Kain–Fritsch convective parameterization: An update. *J. Appl. Meteor.*, **43**, 170–181, doi:10.1175/1520-0450(2004)043<0170:TKCPAU>2.0.CO;2.

Kim, D., C. S. Jin, C. H. Ho, J. Kim, and J. H. Kim, 2015: Climatological features of WRF-simulated tropical cyclones over the western North Pacific. *Climate Dyn.*, **44**, 3223–3235, doi:10.1007/s00382-014-2410-3.

Kummerow, C., and Coauthors, 2000: The status of the Tropical Rainfall Measuring Mission (TRMM) after two years in orbit. *J. Appl. Meteor.*, **39**, 1965–1982, doi:10.1175/1520-0450(2001)040<1965:TSOTTR>2.0.CO;2.

Lee, H.-T., 2014: Climate algorithm theoretical basis document (C-ATBD): Outgoing longwave radiation (OLR)—Daily. NOAA's Climate Data Record (CDR) Program.

NOAA Tech Rep. CDRP-ATBD-0526, 46 pp. [Available online at http://www1.ncdc.noaa.gov/pub/data/sds/cdr/CDRs/Outgoing%20Longwave%20Radiation%20-%20Daily/AlgorithmDescription.pdf.]

Lim, K., and S. Hong, 2010: Development of an effective double-moment cloud microphysics scheme with prognostic cloud condensation nuclei (CCN) for weather and climate models. *Mon. Wea. Rev.*, **138**, 1587–1612, doi:10.1175/2009MWR2968.1.

Mallard, M. S., G. M. Lackmann, A. Aiyyer, and K. Hill, 2013: Atlantic hurricanes and climate change. Part I: Experimental design and isolation of thermodynamic effects. *J. Climate*, **26**, 4876–4893, doi:10.1175/JCLI-D-12-00182.1.

Maloney, E. D., and D. L. Hartmann, 2001: The Madden–Julian oscillation, barotropic dynamics, and North Pacific tropical cyclone formation. Part I: Observations. *J. Atmos. Sci.*, **58**, 2545–2558, doi:10.1175/1520-0469(2001)058<2545:TMJOBD>2.0.CO;2.

Mapes, B. E., T. T. Warner, M. Xu, and A. J. Negri, 2003a: Diurnal patterns of rainfall in northwestern South America. Part I: Observations and context. *Mon. Wea. Rev.*, **131**, 799–812, doi:10.1175/1520-0493(2003)131<0799:DPORIN>2.0.CO;2.

——, ——, and ——, 2003b: Diurnal patterns of rainfall in northwestern South America. Part III: Diurnal gravity waves and nocturnal convection offshore. *Mon. Wea. Rev.*, **131**, 830–844, doi:10.1175/1520-0493(2003)131<0830:DPORIN>2.0.CO;2.

Molinari, J., and D. Vollaro, 2000: Planetary- and synoptic-scale influences on eastern Pacific tropical cyclogenesis. *Mon. Wea. Rev.*, **128**, 3296–3307, doi:10.1175/1520-0493(2000)128<3296:PASSIO>2.0.CO;2.

——, S. Knight, M. Dickinson, D. Vollaro, and S. Skubis, 1997: Potential vorticity, easterly waves, and eastern Pacific tropical cyclogenesis. *Mon. Wea. Rev.*, **125**, 2699–2708, doi:10.1175/1520-0493(1997)125<2699:PVEWAE>2.0.CO;2.

Mozer, J. B., and J. A. Zehnder, 1996: Lee vorticity production by large-scale tropical mountain ranges. Part I: Eastern North Pacific tropical cyclogenesis. *J. Atmos. Sci.*, **53**, 521–538, doi:10.1175/1520-0469(1996)053<0521:LVPBLS>2.0.CO;2.

Nitta, T., and Y. Takayabu, 1985: Global analysis of the lower tropospheric disturbances in the tropics during the northern summer of the FGGE year part II: Regional characteristics of the disturbances. *Pure Appl. Geophys.*, **123**, 272–292, doi:10.1007/BF00877023.

NOAA, 2014: Outgoing longwave radiation—Daily. National Climatic Data Center, accessed 23 June 2014. [Available online at http://www.ncdc.noaa.gov/cdr/operationalcdrs.html.]

Nolan, D. S., 2007: What is the trigger for tropical cyclogenesis? *Aust. Meteor. Mag.*, **56**, 241–266.

Raymond, D. J., C. Lopez-Carrillo, and L. Lopez Cavazos, 1998: Case-studies of developing east Pacific easterly waves. *Quart. J. Roy. Meteor. Soc.*, **124**, 2005–2034, doi:10.1002/qj.49712455011.

——, S. Gjorgjievska, S. L. Sessions, and Z. Fuchs, 2014: Tropical cyclogenesis and mid-level vorticity. *Aust. Meteor. Oceanogr. J.*, **64**, 11–25.

Rydbeck, A. V., and E. D. Maloney, 2014: Energetics of east Pacific easterly waves during intraseasonal events. *J. Climate*, **27**, 7603–7621, doi:10.1175/JCLI-D-14-00211.1.

——, and ——, 2015: On the convective coupling and moisture organization of east Pacific easterly waves. *J. Climate*, **72**, 3850–3870, doi:10.1175/JAS-D-15-0056.1.

——, ——, S. Xie, J. Hafner, and J. Shaman, 2013: Remote forcing versus local feedback of east Pacific intraseasonal variability during boreal summer. *J. Climate*, **26**, 3575–3596, doi:10.1175/JCLI-D-12-00499.1.

Serra, Y. L., G. N. Kiladis, and M. G. Cronin, 2008: Horizontal and vertical structure of easterly waves in the Pacific ITCZ. *J. Atmos. Sci.*, **65**, 1266–1284, doi:10.1175/2007JAS2341.1.

——, ——, and K. I. Hodges, 2010: Tracking and mean structure of easterly waves over the Intra-Americas Sea. *J. Climate*, **23**, 4823–4840, doi:10.1175/2010JCLI3223.1.

Shapiro, L. J., 1986: The three-dimensional structure of synoptic-scale disturbances over the tropical Atlantic. *Mon. Wea. Rev.*, **114**, 1876–1891, doi:10.1175/1520-0493(1986)114<1876:TTDSOS>2.0.CO;2.

Simpson, R. H., N. Frank, D. Shideler, and H. M. Johnson, 1969: Atlantic tropical disturbances of 1968. *Mon. Wea. Rev.*, **97**, 240–255, doi:10.1175/1520-0493(1969)097<0240:ATDO>2.3.CO;2.

Skamarock, W. C., and J. B. Klemp, 2008: A time-split nonhydrostratic atmospheric model for weather research and forecasting applications. *J. Comput. Phys.*, **227**, 3465–3485, doi:10.1016/j.jcp.2007.01.037.

Small, R. J., S.-P. Xie, E. D. Maloney, S. P. deSzoeke, and T. Miyama, 2011: Intraseasonal variability in the far-east Pacific: Investigation of the role of air–sea coupling in a regional coupled model. *Climate Dyn.*, **36**, 867–890, doi:10.1007/s00382-010-0786-2.

Tai, K. S., and Y. Ogura, 1987: An observational study of easterly waves over the eastern Pacific in the northern summer using FGGE data. *J. Atmos. Sci.*, **44**, 339–361, doi:10.1175/1520-0469(1987)044<0339:AOSOEW>2.0.CO;2.

Thompson, G., P. R. Field, R. M. Rasmussen, and W. D. Hall, 2008: Explicit forecasts of winter precipitation using an improved bulk microphysics scheme. Part II: Implementation of a new snow parameterization. *Mon. Wea. Rev.*, **136**, 5095–5115, doi:10.1175/2008MWR2387.1.

Thorncroft, C. D., and K. Hodges, 2001: African easterly wave variability and its relationship to Atlantic tropical cyclone activity. *J. Climate*, **14**, 1166–1179, doi:10.1175/1520-0442(2001)014<1166:AEWVAI>2.0.CO;2.

——, N. M. J. Hall, and G. N. Kiladis, 2008: Three-dimensional structure and dynamics of African easterly waves. Part III: Genesis. *J. Atmos. Sci.*, **65**, 3596–3607, doi:10.1175/2008JAS2575.1.

Toma, V., and P. J. Webster, 2010a: Oscillations of the intertropical convergence zone and the genesis of easterly waves. Part I: Theory and diagnostics. *Climate Dyn.*, **34**, 587–604, doi:10.1007/s00382-009-0584-x.

——, and ——, 2010b: Oscillations of the intertropical convergence zone and the genesis of easterly waves. Part II: Numerical experiments. *Climate Dyn.*, **34**, 605–613, doi:10.1007/s00382-009-0585-9.

Tulich, S. N., G. N. Kiladis, and A. Suzuki-Parker, 2011: Convectively coupled Kelvin and easterly waves in a regional climate simulation of the tropics. *Climate Dyn.*, **36**, 185–203, doi:10.1007/s00382-009-0697-2.

Velasco, I., and J. M. Fritsch, 1987: Mesoscale convective complexes in the Americas. *J. Geophys. Res.*, **92**, 9591–9613, doi:10.1029/JD092iD08p09591.

Warner, T. T., B. E. Mapes, and M. Xu, 2003: Diurnal patterns of rainfall in northwestern South America. Part II: Model simulation and comparison with observations. *Mon. Wea. Rev.*, **131**, 813–829, doi:10.1175/1520-0493(2003)131<0813:DPORIN>2.0.CO;2.

Zuluaga, M. D., and R. A. Houze Jr., 2015: Extreme convection of the near-equatorial Americas, Africa, and adjoining oceans as seen by TRMM. *Mon. Wea. Rev.*, **143**, 298–316, doi:10.1175/MWR-D-14-00109.1.